AIAA JOURNAL
Vol. 35, No. 1, January 1997

Computation of Unsteady Flowfield over a Hydrofoil, Including Boundary Layer and Wake

Y.-H. Ho* and B. Lakshminarayana†
Pennsylvania State University, University Park, Pennsylvania 16802-1400

A time-accurate, two-dimensional, semi-implicit pressure-based Navier–Stokes solver for incompressible flows is used to carry out the numerical simulation of the unsteady flow over a hydrofoil. A low-Reynolds-number form of the two-equation turbulence model is used to account for the turbulence effects. To improve the accuracy of the numerical scheme, a central differencing plus artificial dissipation scheme is implemented to provide a precise control of the numerical dissipation. An inner-loop iteration scheme is used at each time step to account for the nonlinear effects. The information on the upstream time-dependent flow is specified from the experimental data. The results show that the characteristics of the unsteady boundary layers along the foil surfaces are predicted very well by the numerical method, including the amplitude of the velocity fluctuation and the phase angle changes as well as flow features near the surfaces. The instantaneous flowfield is presented at various locations along the hydrofoil surfaces and downstream of the hydrofoil. Both the computational and experimental results are interpreted to improve physical understanding of the flow phenomena inside unsteady boundary layers.

Nomenclature

a^i = influence coefficient; Eq. (6)
C = chord length
C_p = static pressure coefficient
C_μ = model constant in k-ε equation (0.09)
G_1, G_2 = contravariant velocity; Eq. (5)
h = distance from the hydrofoil surface
J = Jacobian
k = turbulence kinetic energy
p = static pressure
p_{ref} = reference pressure (10% chord upstream on the tunnel wall)
S_ϕ = source term
T = period
T_u = turbulence intensity $[\sqrt{(\frac{2}{3}k)}/V_1]$
t = physical time
u, v = axial and transverse velocity
u_i = mean velocity
u_i' = fluctuation velocity
V = total velocity, $\sqrt{(u^2 + v^2)}$
V_s = velocity component parallel to the foil surface
x, z = axial and transverse direction; Fig. 2
x_i, x_j = Cartesian coordinates
y = distance from the wall
y^+ = $\sqrt{\rho (\tau_w/\rho)}\,(y/\mu)$
ΔT_u = first harmonic amplitude of T_u
ΔV_s = first harmonic amplitude of velocity fluctuation
ΔV_{s2} = second harmonic amplitude of velocity fluctuation
ε = turbulence dissipation rate
$\varepsilon_2, \varepsilon_4$ = coefficients of artificial dissipation
μ = molecular viscosity
μ_r = ratio of laminar to turbulent viscosity, μ/μ_t
μ_t = turbulent eddy viscosity
ν = kinematic viscosity
ξ, η = independent variables on transformation plane
ρ = fluid density
τ_w = shear stress on the wall
ϕ = dependent variable u or v in Eq. (5)
Ψ = flow variable in Eq. (9)
ω = radian frequency, s^{-1}

Subscripts

W, E, N, S = surrounding grid-point indices
1 = inlet

Superscript

$(-)$ = time-mean value

Introduction

IT is well known that the steady and unsteady boundary-layer development on the surfaces of hydrofoils and airfoils has a major influence on the steady and unsteady fluid-dynamic, structural, and aeroelastic performance of these hydrofoils or airfoils. Because the boundary layers are thin, it is very difficult to measure or to predict their properties accurately. Most analytical and experimental studies carried out hitherto have focused on the steady-state boundary-layer development. There are very few studies that address the effects of freestream unsteadiness on the airfoil boundary layer. The unsteady effects usually result in a very complex flowfield, with amplitude and phase changes in velocity components and turbulence quantities within the boundary layer. Well-controlled experiments should be able to resolve various features of unsteady viscous flows and provide databases for the validation of a Navier–Stokes code.

Many experiments on the unsteady boundary layers have been conducted over the past 20 years, typical examples being those of Patel,[1] Cousteix and Houdeville,[2] and Brendel and Mueller.[3] They were able to measure the unsteady velocity profiles and phase angles inside the boundary layers. Typical examples of unsteady flow computations were performed by Huff,[4] Scott and Atassi,[5] and Ghia et al.[6] Very few attempts have been made to predict the unsteady boundary layers on an airfoil and to assess the ability of Navier–Stokes solvers to predict the unsteady viscous flowfield. Hence, the main objective of this study is to develop an accurate and efficient Navier–Stokes solver to predict the unsteady boundary layer on a hydrofoil, including the unsteady pressure and the unsteady velocity. The second objective is to understand the mechanism and physics of an unsteady viscous flowfield through numerical simulation. The main contributions of this research can be summarized as follows:

1) The successful adaptation of a SIMPLE-type algorithm to predict two-dimensional unsteady flows, including unsteady pressure

Received April 3, 1995; revision received April 29, 1996; accepted for publication Aug. 13, 1996; also published in *AIAA Journal on Disc*, Volume 2, Number 1.

*Graduate Student, Department of Aerospace Engineering. Student Member AIAA.
†Evan Pugh Professor, Department of Aerospace Engineering, and Director, Center for Gas Turbines and Power, 153 Hammond Building. Fellow AIAA.

on the hydrofoil surfaces, unsteady boundary layers, and unsteady wakes. The code was validated against benchmark quality data by Keenan et al.[7]

2) Implementation of an explicit artificial dissipation for unsteady flows in a pressure-based technique. This provides a precise control of the numerical dissipation while maintaining the numerical stability.

3) Provide detailed information and interpretation of unsteady viscous flows near a hydrofoil surface. Some of the details (such as turbulence structure) were neither available nor can be measured during experiment.

The case studied here is the unsteady flow over a hydrofoil due to two upstream flapping foils. The experiments were conducted by Keenan et al.[7] in a water tunnel at Massachusetts Institute of Technology (MIT). This is one of the benchmark quality experimental data available on unsteady boundary layers. Detailed measurement of the unsteady boundary-layer properties were carried out at several axial locations along the hydrofoil surfaces using laser Doppler velocimetry (LDV).

Numerical Technique

The Reynolds-averaged Navier–Stokes equations for two-dimensional, unsteady, incompressible flow in Cartesian tensor form can be written as

$$\frac{\partial u_i}{\partial x_i} = 0 \tag{1}$$

$$\frac{\partial u_i}{\partial t} + \frac{\partial u_i u_j}{\partial x_j} = -\frac{1}{\rho}\left\{\frac{\partial p}{\partial x_j} - \frac{\partial}{\partial x_j}\left[\mu\left(\frac{\partial u_j}{\partial x_i} + \frac{\partial u_i}{\partial x_j}\right) + \rho\overline{u_i' u_j'}\right]\right\} \tag{2}$$

where x_i are the independent variables, ρ is the mean density, and u_i' is the fluctuation velocity about the mean. To simulate the turbulent flow, a two-equation, or k-ε, turbulence model by Chien[8] is employed.

The boundary conditions include no-slip condition on the solid surfaces and specification of time-dependent inlet velocity field. The exit velocity is computed by applying the governing equation directly at the exit. Slip boundary conditions are applied to the upper and lower walls, i.e., all flow properties on the upper and lower walls of the tunnel are set equal to the quantities at the grid points below or above the walls. This was intended to allow for wall effects without using excessive numbers of grid points to resolve the boundary layers on the test-section walls.

For the pressure equation, the normal derivative of the static pressure is assumed to be zero at the solid surface, which is a reasonable approach for high-Reynolds-number flows. The static pressure is specified at the exit plane. At inlet, the streamwise pressure gradient is set to zero. Because Neumann boundary conditions are used, the pressure at one grid point must be chosen. This control point is taken to be the midchannel point at the exit plane.

The values k and $\varepsilon = 2\nu k/y^2$ (the asymptotic value of ε near the wall, see Ref. 9 for further details) are set to zero at the wall for the k-ε equations. The inlet turbulent kinetic energy and dissipation rate are determined by specifying an inlet turbulence intensity T_u and the turbulent viscosity ratio factor μ_r associated with the inlet flow. The inlet turbulent kinetic energy is determined from

$$k_1 = \tfrac{3}{2}(T_u V_1)^2 \tag{3}$$

where V_1 is the inlet total velocity. The inlet dissipation rate then is determined from the following relation:

$$\varepsilon_1 = \rho_1 C_\mu \frac{k_1^2}{\mu_t} \tag{4}$$

The k and ε at the exit plane also are calculated by applying the transport equations directly.

A control-volume approach is used in the discretization procedures for the system of governing equations. The detailed procedure can be found elsewhere.[10,11] Second-order and fourth-order artificial dissipation terms are added explicitly to control the numerical dissipation. The expression for the second-order and the fourth-order dissipation can be represented by

$$+\frac{1}{2}\varepsilon_2\left[\Delta\xi\frac{\partial}{\partial\xi}\left(|\rho J G_1|\frac{\partial\phi}{\partial\xi}\right) + \Delta\eta\frac{\partial}{\partial\eta}\left(|\rho J G_2|\frac{\partial\phi}{\partial\eta}\right)\right] - \frac{1}{8}\varepsilon_4\left[\Delta\xi^3\frac{\partial}{\partial\xi}\left(|\rho J G_1|\frac{\partial^3\phi}{\partial\xi^3}\right) + \Delta\eta^3\frac{\partial}{\partial\eta}\left(|\rho J G_2|\frac{\partial^3\phi}{\partial\eta^3}\right)\right] \tag{5}$$

where ε_2 and ε_4 are the coefficients of the second-order and fourth-order dissipation terms; $\Delta\xi$ and $\Delta\eta$ are the grid spacing in ξ and η directions. For unsteady flow computations, ε_2 is set to zero and ε_4 is set to 0.25. These values are chosen on the basis of extensive parametric studies and were reported by Ho.[10]

A fourth-order artificial dissipation also is added to the pressure equation to prevent pressure oscillation. This is sufficient to provide a smooth pressure field. For temporal discretization, a backward-differencing implicit scheme is selected. Thus, the second-order accuracy in time domain is preserved. The diffusive terms are approximated by the central differencing scheme. All cross derivatives are treated explicitly and are considered as source terms.

The numerical scheme used in this work is the modified version of pressure-implicit with splitting of operators (PISO) scheme developed by Issa.[12] Detailed implementation of this algorithm and its modifications can be found elsewhere.[10] To take into account the coupling between the governing equations and the turbulence model, an inner iteration loop is introduced in the original scheme to account for the nonlinear interaction between the flowfield and the turbulence. The discretized form of the general transport equation can be written first as

$$(3\rho J/2\Delta t + a^P)\phi_P = a^E\phi_E + a^W\phi_W + a^N\phi_N + a^S\phi_S + S_\Phi \tag{6}$$

where Δt is the time step.

The influence coefficients a^i are first evaluated from the previous time-step solution. To incorporate the nonlinear effects, the discretized Eqs. (6) are modified, by using the idea of Van Doormaal and Raithby,[13] as

$$(3\rho J/2\Delta t + a^P)^*\phi_P = a^E\phi_E + a^W\phi_W + a^N\phi_N + a^S\phi_S + (S_\phi)^* \tag{7}$$

where ϕ_P^* is the current estimate of ϕ_P for advancing in time and

$$(3\rho J/2\Delta t + a^P)^* = (3\rho J/2\Delta t + a^P)[1 + (1/E_R)]$$

$$(S_\phi)^* = S_\phi + \frac{(\rho 3J/2\Delta t + a^P)}{E_R}\phi_P^*$$

E_R is chosen so that the diagonal dominant solution matrix is maintained. Van Doormaal and Raithby[13] showed that the limit of E_R is 1 for an explicit scheme. Because the time step Δt is usually small in time-accurate computations, the value of E_R can be larger than 1. As shown in Eq. (7), if time-dependent terms are removed, the original E-factor scheme is recovered. This E-factor scheme is implemented in the inner iteration loop to update the influence coefficients a^i and ϕ_i during each time step. At convergence of Eq. (7), the influence coefficients and the variables are coupled in the time-accurate solutions. The inner iteration is continued until the following convergence criteria are satisfied or 25 inner iterations are achieved in computations:

$$\frac{|R_\phi^{**} - R_\phi^*|}{R_\phi^*} < \text{tolerance}, \qquad R_m^{**} < \text{tolerance} \tag{8}$$

where R_ϕ^{**} is the rms residual of variable ϕ at iteration level ** and R_m^{**} is the mass residual. The typical tolerance level for all variables is 1×10^{-3} for rms residual of variables and 1×10^{-6} for mass residual. For an unsteady flow calculation, the initial condition used is the steady-state solution for the same configuration.

As shown elsewhere,[14–16] the two-equation turbulence models can be used to predict unsteady boundary-layer flows at low frequency range because the turbulence can be regarded as in a quasisteady state. Cousteix and Houdeville[2] used a steady wall function with a high-Reynolds-number k-ε model for a periodic turbulent boundary layer. Similarly, Mankbadi and Mobark[16] used a high-Reynolds-number k-ε model and steady wall functions to predict pipe and boundary-layer flows. It has been found that the accuracy of the model deteriorates with increasing level or rate of unsteadiness. Low-Reynolds-number form turbulence models seem to be necessary for accurate prediction of unsteady turbulent wall bounded flows where the near-wall physics is of interest. The applicability of the low-Reynolds-number k-ε models to unsteady flows has been investigated by Justesen and Spalart[14] for an oscillatory turbulent boundary layer with a zero mean velocity. Two different low-Reynolds-number k-ε models are used.[8,17] Comparison with large eddy simulation data indicates that Jones and Launder's[17] model performs better than Chien's[8] model. As pointed out by Patel et al.,[9] Chien's turbulence model was asymptotically consistent in the near-wall region. Therefore, it is argued that the near-wall turbulence can be represented by low-Reynolds-number k-ε model with reasonable accuracy for low frequency flows. Figure 1 shows the unsteady boundary-layer simulations by Fan and Lakshminarayana[18] utilizing the low-Reynolds-number k-ε model. The data were acquired by Patel[1] in a boundary layer subjected to oscillatory freestream. Comparisons are made at three different streamwise locations of the boundary layer. The agreement between the predicted and the measured distributions of amplitude and phase angle of unsteady velocity is generally very good at all three streamwise locations. A discussion on timescales of mean flow, gust, turbulence, and the numerical time steps needed to resolve these flows for a specific case used in this paper is given in the next section.

A systematic approach has been taken during the course of this Navier–Stokes code development. The main features and uniqueness of this approach can be summarized as follows (details can be found in Ref. 10):

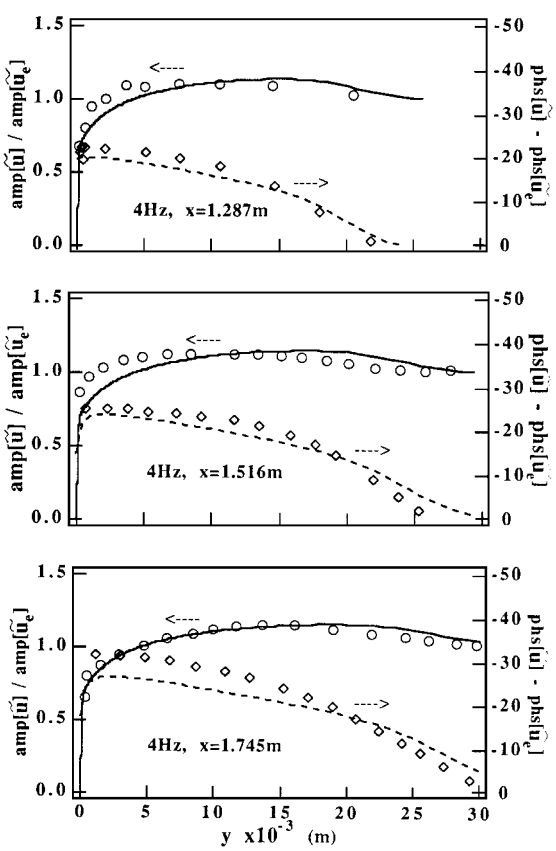

Fig. 1 First Fourier component of velocity profile for an unsteady boundary layer: symbols, data[1]; lines, prediction.[18] $\tilde{u}$ and $\tilde{u}_e$ are local and freestream ensemble averaged velocities, respectively.

1) Second-order and fourth-order artificial dissipation schemes were implemented in the code to provide a precise control of the numerical dissipation.

2) Analytical and numerical study was made of the effects of the artificial dissipation on unsteady flows over a wide range of reduced frequencies to optimize the code for accuracy and stability.

3) Enhanced coupling between the mean flow and the turbulence was accomplished by incorporating inner iteration loops in the numerical technique.

4) Several computational grids were generated and a grid dependency study was performed to ensure that the solutions were independent of the grids. The effects of the numbers of time steps on flow solutions also were studied to resolve proper timescales in the mean flow and in turbulence structure.

5) Unsteady viscous flow over a hydrofoil is simulated and validated against available data. A detailed interpretation on the physics of the flow is carried out, based on additional simulation for which data are not available.

Computational Simulation and Comparison with Data

Description of Test Case and Numerical Model

The test case chosen here is the experiment conducted by Keenan et al.[7] Detailed measurements of the instantaneous velocity field in the freestream and in the boundary layers were acquired at several axial locations. Two-component LDV was used for velocity data at positions away from the foil. In the boundary layer and near wake, a one-component setup was used. Static pressures on the hydrofoil surfaces were measured at discrete points, not as distributions. The hydrofoil had a typical cross section of blades used in marine propulsors. Its chord length was 0.4572 m and it had an angle of attack of 1.18 deg. The locations of two flapping foils used to generate unsteady gusts are at 0.8 chord length upstream of the hydrofoil and 0.28 chord length above and below the test foil in the crossflow direction. A sketch of the experimental layout is shown in Fig. 2. The test Reynolds number is 3.78×10^6 based on the hydrofoil chord length and the tunnel flow speed. The unsteady flow is generated by flapping two foils synchronously at an amplitude of 6 deg about their own geometric centers. The flappers operated at a reduced frequency ($\omega C/2V_1$) of 3.62. The boundary layers are tripped at an axial location of 0.1 chord downstream of the leading edge. This ensures a fully turbulent flowfield along the blade surfaces. Time-dependent velocity fields were measured at 13 locations along the transverse direction to define the inflow conditions (line AD in Fig. 2). Thirty-six locations along the measurement box, shown in Fig. 2, were chosen to describe the freestream unsteady flowfield. For the unsteady boundary-layer measurements, the time-dependent velocity was acquired at five locations on the suction surfaces and three locations on the pressure surface.

The computational domain (marked ABCD in Fig. 2) is extended to the upper and lower tunnel walls. The inlet plane is chosen at an axial location of 0.26 chord upstream, where detailed flow data, including the instantaneous axial and tangential velocity components, are available. The exit plane is chosen at 0.9 chord downstream of the hydrofoil. An H-type grid is used to discretize the computational domain. The computational grid consists of 201 grid points in the axial direction and 137 grid points in the tangential direction. To resolve the boundary-layer characteristics, the grid is constructed to ensure that at least 20 grid points are located inside the boundary layers and the y^+ value is less than 1 for the first grid point away from the blade surfaces.

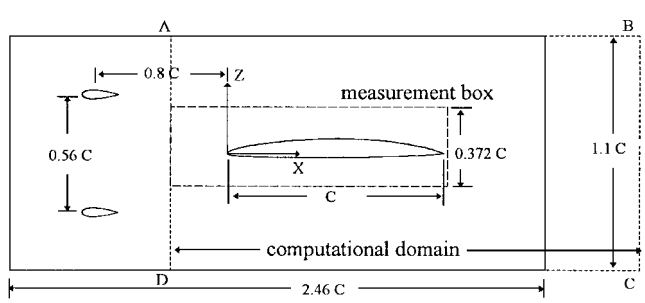

Fig. 2 Test setup for the MIT flapping foils experiment.

At the inlet plane (AD in Fig. 2), 13 measured locations have been utilized to linearly interpolate and extrapolate the inlet velocities. A cubic spline algorithm is used to smooth the experimental data in the time domain. Snapshots of the instantaneous velocity distributions at the inlet plane are shown elsewhere.[10] The gust is found to have appreciable fluctuations in both the transverse (z) and streamwise (x) directions. Grid points are clustered near the inlet plane to account for these high instantaneous velocity gradients present at the inlet boundary. Inlet turbulence intensity is set to be 1% according to Keenan et al.[7] To assess the effects of turbulence on the flow characteristics, two additional levels of inlet turbulence intensity, 2 and 5%, were used in the steady-state computations, with no noticeable difference in steady velocity distribution.

To ensure that the timescale was resolved properly, various time steps per cycle were used to carry out the unsteady flow simulation. The time history of the total force on the hydrofoil surface was monitored with different time steps per period. There was no noticeable change between 250 and 500 time steps per period. The results shown in this paper are based on 500 time steps per period. This represents a physical time step of 2×10^{-5} s. The timescales of the flow are 0.053 s for the mean flow and 0.01 s for the gust. The estimated timescales for the largest eddy (equal to the boundary-layer thickness) is 10^{-3} s and the smallest eddy is 6×10^{-5} s. It is thus clear that the time step chosen should be able to capture all flow and turbulence features, within the accuracy of the turbulence model employed.

The experimental program covered a wide range of instantaneous velocity measurement in the flowfield. The predicted velocity components are compared to data at various locations in the flowfield along the measurement box (see Fig. 2). The axial coordinate (x) is positive downstream. The origin of the coordinate is located at the leading edge of the hydrofoil. Z denotes the crossflow direction and is positive upward, as shown in Fig. 2.

This set of experimental data was chosen as a blind test case by the Office of Naval Research for evaluation in a workshop held in 1993. About six to eight groups were asked to compute this flow (with only geometry and boundary conditions provided), and the blind results were submitted to Navy personnel for evaluation. Information about the workshop and assessment is summarized by Fuhs.[19] Various numerical techniques and turbulence models were employed, including time-marching and pressure-based techniques. The results indicated that the numerical technique presented in this paper provided good unsteady flow simulation of this case.

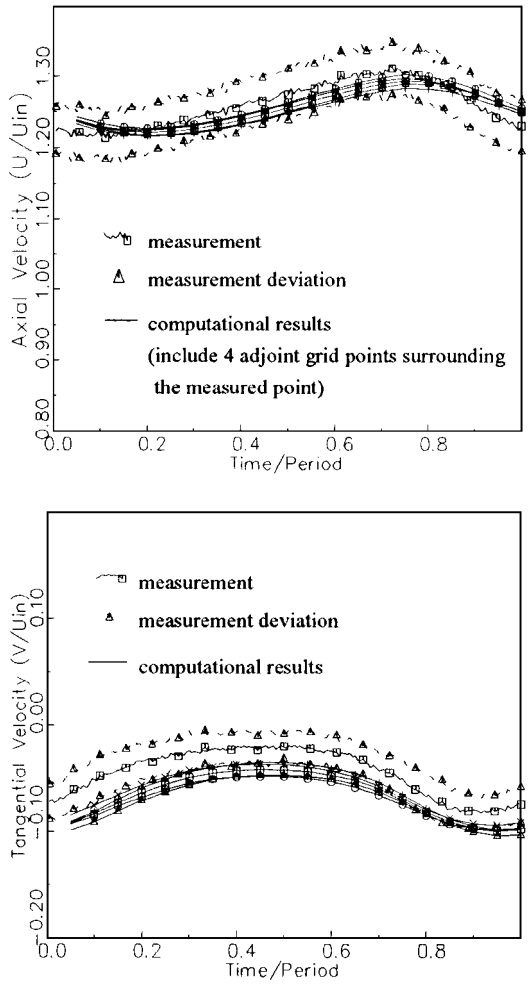

Fig. 3 Time-dependent velocity components at location $x/C = 0.6524$ and $z/C = 0.2187$.

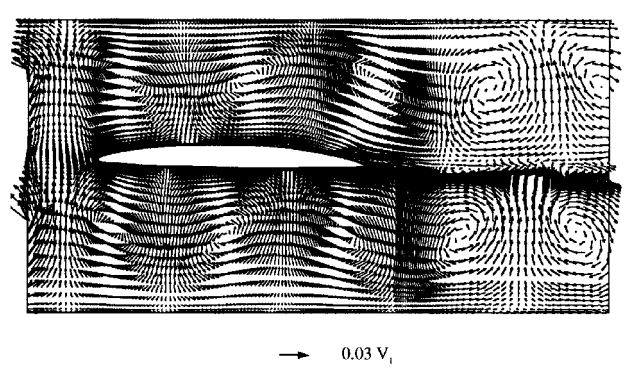

Fig. 4 Instantaneous unsteady velocity vector $[V(t) - \bar{V}]$ over the hydrofoil at $t/T = 0.6$.

Unsteady Flowfield in the Freestream

An assessment of the accuracy of the numerical simulation of the freestream flowfield is presented in Fig. 3 for one typical location ($x/C = 0.6524$ and $z/C = 0.2187$). The numerical simulation is able to capture both the magnitude and the phase angle of the velocity components, similar agreement is obtained at various axial and transverse locations away from the hydrofoil.[10] The wave motions due to the vortices generated by upstream flapping foils are captured and the inviscid part of the flowfield is simulated with very good accuracy. The complexities of this flowfield can also be observed. Not only the streamwise gust but also the transverse gust is present in this flowfield; the magnitudes of the gusts are significant, as much as 10% of the inlet freestream velocity at some locations.

Unsteady velocity vectors at $t/T = 0.6$ are shown in Fig. 4. The pairing vortices generated by the flapping foils are convected downstream in the inviscid region, without much decay. Because of the flow acceleration in the contraction region (the region above the foil suction surface), the vortex in the upper region travels faster than the one on the lower side. As many as six vortices can be found in the computational domain on both sides of the hydrofoil at a reduced frequency of 3.62. These vortices not only interact with the boundary layer to create the flow patterns as described later, they also interact with the wake downstream of the foil. The gust structure varies substantially in the crossflow direction, but its salient feature is that in the nominal plane of the test foil it has virtually no streamwise component and is almost all crossflow. Thus, in a linearized sense, we have a propagating transverse gust, i.e., the Sears problem.

Several mechanisms responsible for the unsteady pressure and the unsteady boundary layers on the hydrofoil surfaces can be recognized from this plot: the incidence change upstream of the hydrofoil due to the transverse gust, the change due to fluctuations in streamwise velocity both upstream and on the hydrofoil, and the periodic variation of the downstream flowfield. The last two mechanisms have not been recognized in the earlier studies of unsteady flows. The periodic variation in the freestream velocity and its impact on the boundary-layer flow should be recognized in evaluating the fluctuating processes as well as the unsteady boundary-layer growth. This is covered in detail later in this section. All of these mechanisms are important in assessing the unsteady performance of airfoils and hydrofoils.

Steady and Unsteady Blade Static Pressure

The time-mean static pressure distributions on the hydrofoil surfaces, compared with the experimental data from the static pressure

holes as well as the data derived from the velocity measurement, are shown in Fig. 5. All of the computations[19] of the surface static pressure were nearly identical, with the same deviation between the data and the prediction near the trailing edge of the suction surface. The concern was that the derived static pressure is probably more accurate. If the boundary-layer approximation (constant static pressure across the boundary layer) is used, one can apply the Bernoulli equation at the edge of the boundary layer. The static pressure on the hydrofoil thus was derived from the velocities measured at the edge of the boundary layer. Both data are shown in Fig. 5. The prediction is in better agreement with the derived static pressure than that measured from static pressure holes, especially on the suction surface. Significant adverse pressure gradients exist in the aft 15% chord length on the suction surface. As shown later, this high adverse static pressure gradient contributes to the rapid development of the boundary layer on the hydrofoil in this region.

The amplitude of the first harmonic of the static pressure on the foil surface is presented in Fig. 6. The corresponding phase-angle changes are shown in Fig. 7. All harmonic components presented here are based on the following:

$$\Psi = \Psi_0 + \sum_{n=1}^{\infty} \Psi_n \sin(n\omega t + \varphi_n) \tag{9}$$

where subscript 0 represents the time-mean value, subscript n the harmonic n, and φ the phase angle. All of the phase calculations are referenced to the motion of the flapping foils. When the flapping foils are at 0-deg angle of attack, the phase angle is 0 deg. A phase angle of 90 deg corresponds to the maximum angle of attack of the flapping foils, 6 deg. The phase angle changes from −180 to +180 deg.

A large amplitude of the first harmonic is predicted at the leading-edge region of the hydrofoil, and its magnitude decreases very rapidly along the foil. Even though data are not available near the leading edge for this configuration, the trend predicted is consistent

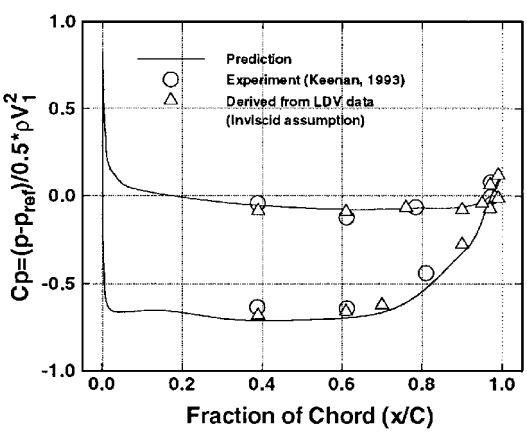

Fig. 5 Time-mean C_p along the hydrofoil surface.

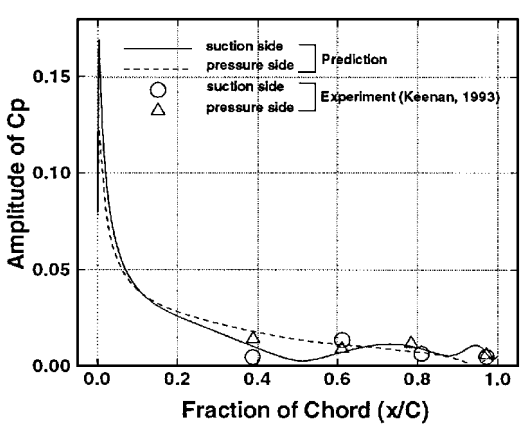

Fig. 6 Amplitude of the first harmonic of C_p on the hydrofoil surface.

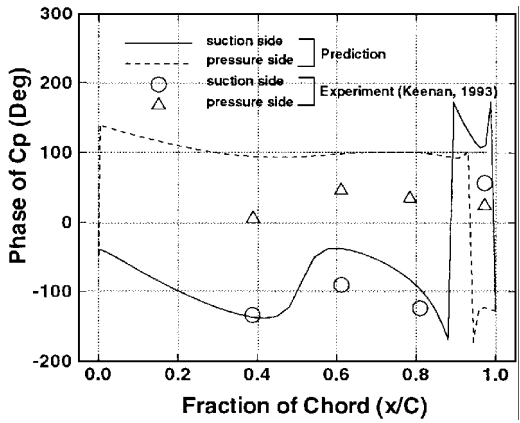

Fig. 7 Phase angle of the first harmonic of C_p on the hydrofoil surface.

with other data and analysis.[19] The numerical model predicts a second peak in the amplitude between 60 and 70% chord on the suction side, which is in good agreement with the data. This phenomenon could be due to the presence of interacting vortices on either side of the gust, as explained in the next section. The velocity profiles on the suction surface also indicate rapid boundary-layer growth starting from this location. Even though the predicted location of the peak of the amplitude is off by about 7% chord, it is very encouraging that the numerical simulation is able to capture the amplitude in this region with reasonable accuracy. The phase angle shown in Fig. 7 also reveals a large phase shift at about 60% chord on the suction surface. The phase angle is one of the most difficult quantities to compute. The accuracy depends on the gust decay as well as the gust convection velocity. Very few investigators have predicted the phase angle to the same accuracy as that shown in Fig. 7 for the suction surface. The pressure surface boundary layers are very thin; this may account for numerical inaccuracy due to grid resolution. Changes in phase angle near the trailing edge are attributed to the small amplitudes of the unsteady static pressure in this region and the numerical inaccuracy associated with the calculation of phase angle for very weak waves. Such error exists in both the data and the computation. For the unsteady lift coefficient, the analysis of a two-dimensional potential-based panel method was used by MIT personnel.[7,20] This analysis results in an amplitude of the lift coefficient of 0.027, whereas the predicted magnitude is 0.030. This reveals that the present numerical procedure is able to predict the unsteady pressure, both the amplitude and the phase angle, accurately.

Time-Mean and Unsteady Boundary Layers

Typical time-mean velocity profiles at various locations along the hydrofoil surfaces are presented in Fig. 8. The velocity component parallel to the surfaces, V_s, is used for this comparison. The results shown in Fig. 8, as well as the comprehensive comparison of Ho,[10] indicate very good agreement with the experimental data at all locations. The experimental data indicate a tendency for the flow to separate at 97% chord, and the numerical simulation does not capture this feature accurately. The hydrofoil was designed to have a zero-thickness trailing edge (used in the computation), which is very difficult to achieve in the manufacturing process. This may account for some of the discrepancy.

The amplitude and phase angle of the unsteady velocity in the foil boundary layers along the hydrofoil surfaces are presented in Figs. 9 and 10. The amplitudes of the unsteady velocity inside the boundary layers are substantial in this case. Their magnitudes vary from 2 to 3% compared to 7% in the freestream (Fig. 3). See Ho[10] for comparison at other chordwise locations. Complex profiles of amplitude and phase angles are captured reasonably well. The amplitude on the suction surface (to some extent, pressure surface) indicate unusual behavior. The amplitude has a peak inside the boundary layer, with a second minimum (dip) near the edge of the boundary layer. This is more pronounced toward the trailing edge. This phenomenon also has been observed by Patel.[1] The computational results predict the locations of maximum and minimum amplitude very well. Considering the uncertainty band of the measurement (see Fig. 3), the

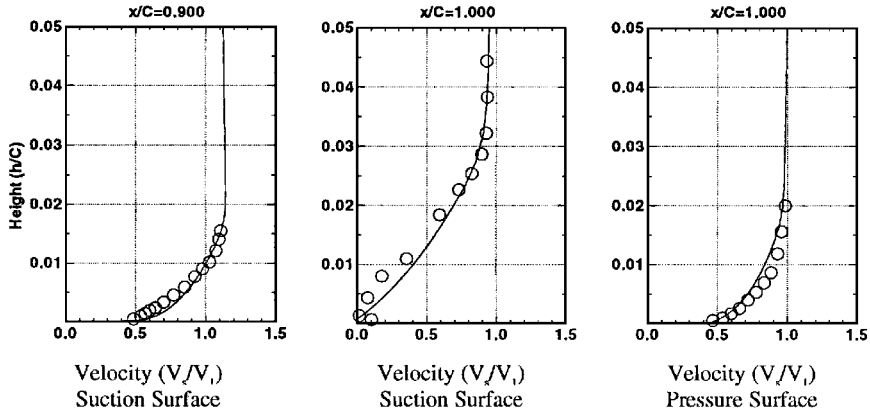

Fig. 8 Time-mean velocity on the surfaces of the hydrofoil (symbol, experimental data,[7,20]; and solid line, numerical prediction).

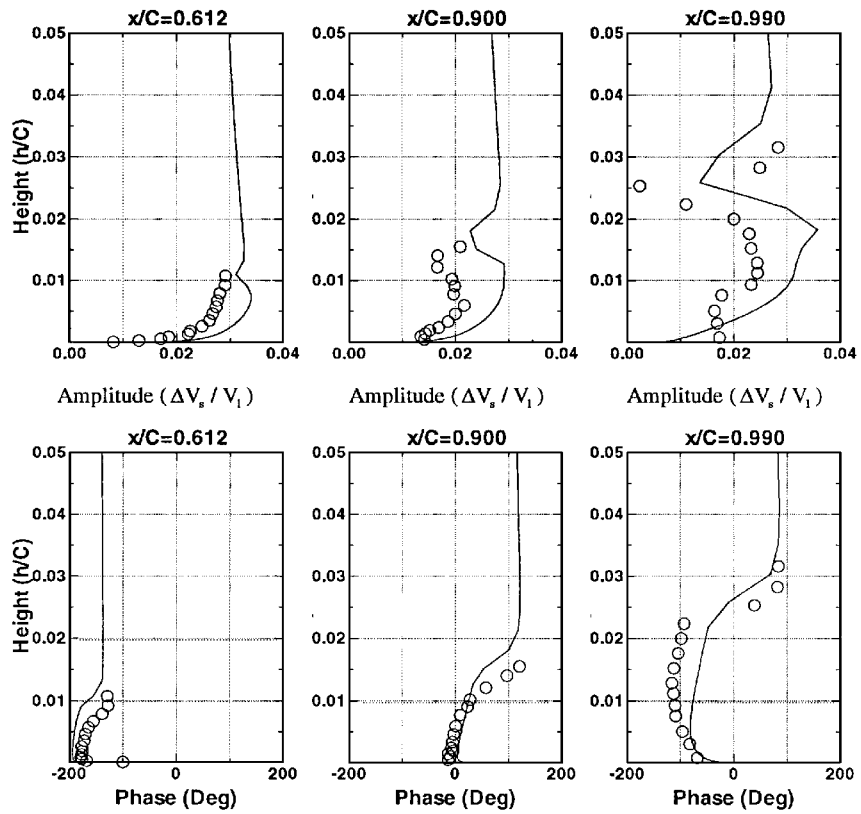

Fig. 9 Amplitude and phase of the first harmonic of unsteady velocity on the hydrofoil suction surface (symbol, experimental data,[7,20]; and solid line, numerical prediction).

amplitudes are captured well. The phase angle is predicted well, including the jump in phase in the outer edge near the trailing edge. This provides confidence in the code. The numerical dissipation and diffusion are minimal, as indicated by these plots.

Large phase-angle changes are observed, both experimentally and computationally, at the edge of the boundary layers, especially near the trailing edge. The phase angles change by as much as 150–160 deg at the trailing-edge region (Figs. 9 and 10). This phenomenon can be explained on the basis of the unsteady velocity vectors shown in Fig. 11. The unsteady velocity is defined as the difference between the instantaneous velocity and the local time-mean value. The shear effect between the unsteady flow inside the boundary layer and that of the freestream can be seen clearly in this plot. The unsteadiness in the freestream is caused by the upstream flapping foils. On the other hand, the unsteady boundary-layer development is influenced by the freestream unsteadiness as well as the unsteady blade pressure, which has a phase lag with the freestream. The interaction of the vortices inside the boundary layers with the freestream gust reduces the influence at the edge of the boundary layer, resulting in lower amplitude of the velocity fluctuations there and a jump in the phase angle (Figs. 9 and 10).

To further investigate the nature of unsteady boundary-layer behavior, the time history of the predicted and measured velocity (V_s/V_1) inside the boundary layers is shown in Fig. 12 for $x/C = 1.0$ for the pressure surface and in Figs. 13 and 14 for $x/C = 0.612$ and 1.0, respectively, for the suction surface. The scales for the results shown in Fig. 13 are kept different intentionally. It is intended to show the flow pattern in the freestream, which was not measured. All other data are plotted to the same scale. Two very distinct flow patterns on either side of the boundary layers can be identified from this series of total velocity time history. First, the freestream flow variations are dominated by the unsteady flows generated from the upstream flapping airfoils. Its wave pattern is very similar to that of the measured flowfield at the inlet plane. As shown in the numerical prediction in Fig. 13, sine waves are clearly seen outside the boundary layer (the edge is located approximately at $h/C = 0.012$ at this axial location). The contours of instantaneous velocity are sheared into a thumbnail pattern near the boundary-layer edge. This

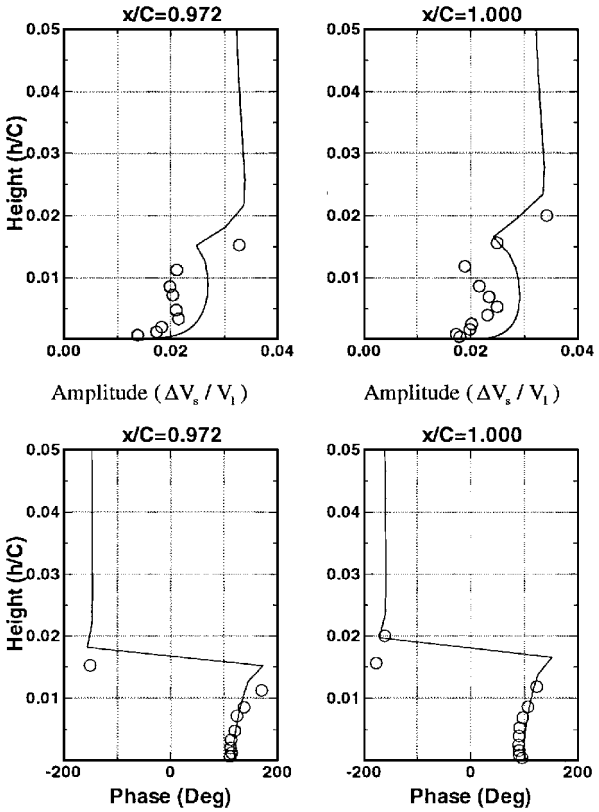

Fig. 10 Amplitude and phase of the first harmonic of unsteady velocity on the hydrofoil pressure surface (symbol, experimental data[7,20]).

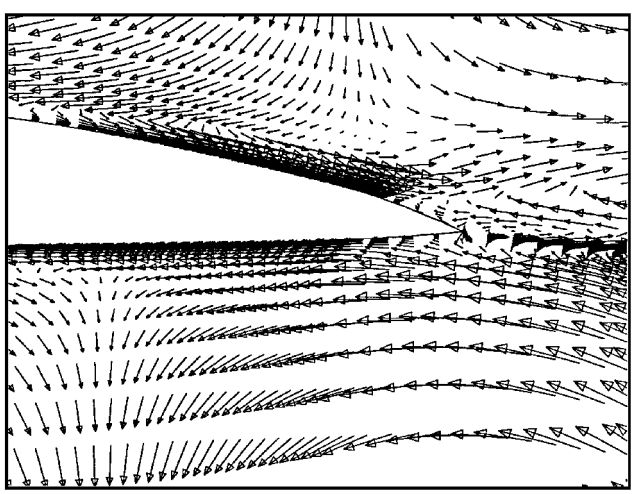

Fig. 11 Instantaneous unsteady velocity [$V(t) - \bar{V}$] vector plot at the hydrofoil trailing edge ($t/T = 0.2$).

indicates that the freestream unsteady flow pattern is not able to penetrate through the boundary layer. Unsteadiness inside the boundary layers is mainly caused by the unsteady pressure and the recirculation pattern set up by the vortices. As the flow travels along the foil surfaces inside the boundary layers, the magnitude of the velocity fluctuation also increases. Because the unsteadiness is convected by the local velocity, the unsteadiness inside the boundary layer travels at a much lower speed compared to that of the freestream. This phase lag between these two flow patterns causes the reduced unsteadiness at the edge of the boundary layers (Figs. 9 and 10).

Although the pressure differences are small near the trailing edge, the excitation in the freestream starts to influence the unsteadiness inside the boundary layers. This phenomenon can be seen from the additional peak appearing near the edge of the boundary layers on both surfaces at the trailing edge (Figs. 9 and 10). Good agreement between the data and prediction at this location indicates that

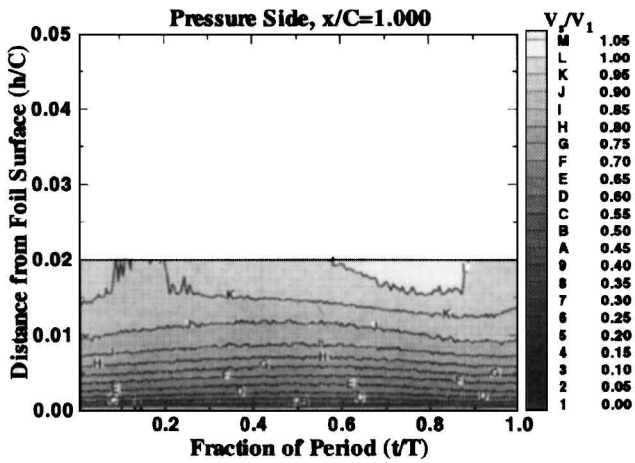

Experimental data[7]

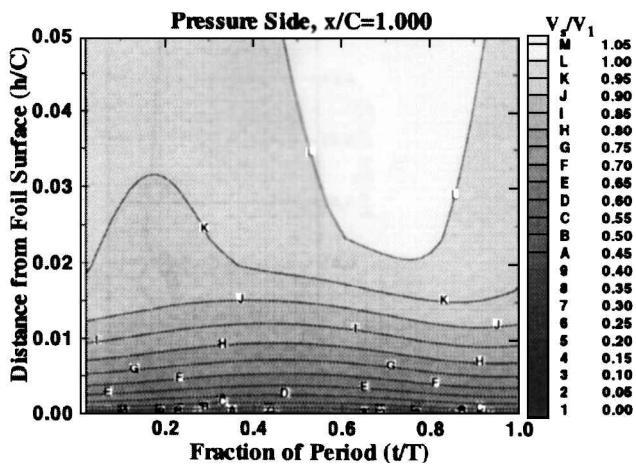

Prediction

Fig. 12 Comparison of time history of the velocity on the hydrofoil pressure surface.

the code is able to capture the unsteadiness arising from complex mechanisms, giving confidence in the numerical simulation.

The amplitude of the second harmonic of velocity fluctuations inside the boundary layers, shown in Fig. 15, reveals that a decrease in magnitude of the first harmonic on the pressure surface [$x/C = 0.972$, $h/C = 0.015$ (Fig. 10)] and on the suction surface [$x/C = 0.99$, $h/C = 0.025$ (Fig. 9)] is accompanied by an increase in the magnitude of the second harmonic at the same location. This indicates that partial energy has been transferred to the higher-frequency domain. Both the experimental data and the simulation show the same trend. It is also clear that the first harmonic dominates inside the boundary layer, except near the edges.

Time-Mean and Unsteady Wake

The time-dependent velocity measurement for the wake flowfield is not available. Thus, the time-mean velocity distributions downstream of the hydrofoil (wake) are presented in Fig. 16a and compared with the available steady-state measurement by Keenan et al.[7] The locations of the predicted maximum velocity defect are slightly off compared to the experimental data. Again, this may be due to the trailing-edge region not being modeled properly, as described earlier. The wake profile and its decay characteristics are captured reasonably well. Figure 16b shows the amplitude of the velocity fluctuations in the wake regions. The unsteadiness inside the boundary layers is carried farther downstream into the wake. Their magnitude remains about the same level even at 50% chord downstream of the hydrofoil. The peak amplitudes occur on both the suction and the pressure sides of the wake away from the wake center. This is caused by the mixing process. One of the interesting phenomena can be observed from the simulation shown in Figs. 16b and 16c. The minimum amplitude on the suction side at $x/C = 1.00$ occurs near

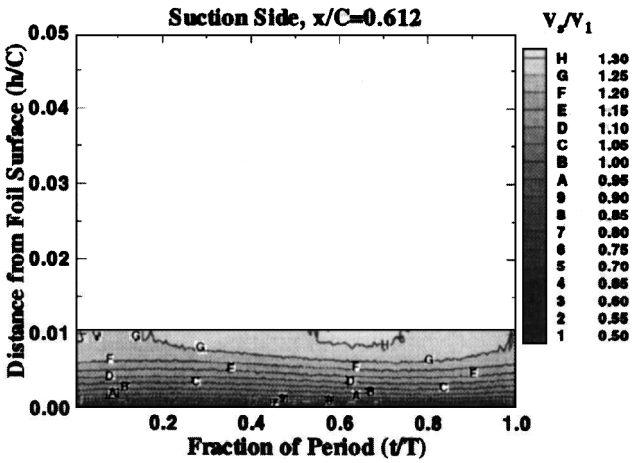

Experimental data[7]

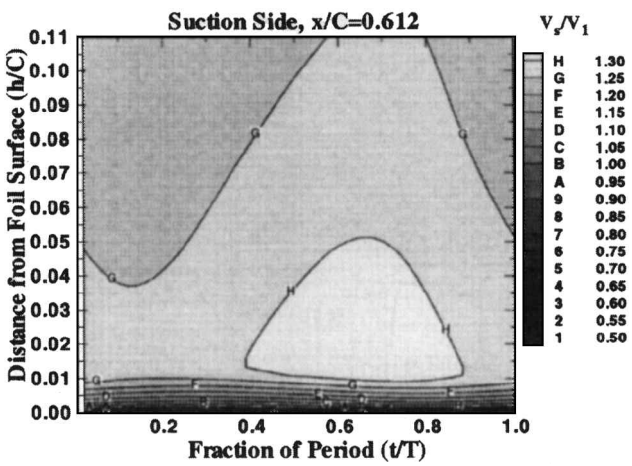

Prediction

Fig. 13 Comparison of time history of the velocity on the hydrofoil suction surface.

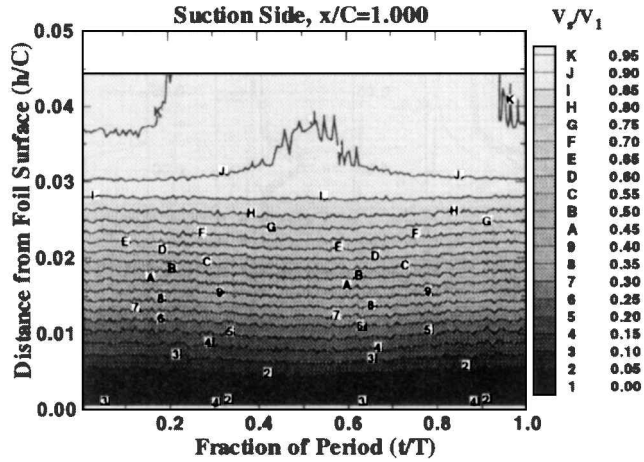

Experimental data[7]

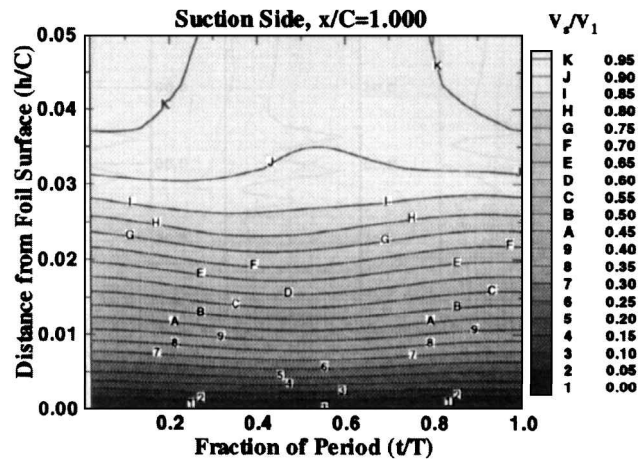

Prediction

Fig. 14 Comparison of time history of the velocity on the hydrofoil suction surface.

$z/C = 0.025$, and this minimum amplitude location moves continuously toward the wake center (Fig. 16b) as the wake progresses downstream. In addition, the magnitude of the minimum amplitude also decreases as the wake travels downstream. This indicates that the freestream unsteadiness penetrates deeper into the inner viscous layer as the flow progresses downstream.

The unsteadiness at the center of the wake increases with the downstream distance. Some interesting conclusions can be drawn from the predicted phase-angle distributions (no data available). The phase angle shows a large jump across the wake near the trailing edge. As explained in the preceding section, this is caused by the differences in gust convection velocity between the pressure and suction surfaces. These differences decrease as the wake travels downstream, even though there is substantial variation in phase angle inside the wake even at 50% chord downstream.

The time history of the velocity in the wake at two locations is illustrated in Fig. 17. The unsteadiness inside the wake region has larger magnitude on the pressure side than on the suction side (as clearly shown in Fig. 16). The two pairs of opposite-rotation vortices downstream of the hydrofoil create a small unsteady recirculation zone between them. Unsteadiness inside this zone is very similar to that observed inside the boundary layers. They tend to be isolated from the inviscid region. This behavior suggests the importance of viscous effects in unsteady flow development.

Turbulence Kinetic Energy Distribution Inside the Boundary Layers and in the Wake

No data are available on the turbulent kinetic energy; hence the simulation results presented here are interpreted to understand the nature of turbulence in the unsteady boundary layer and wake flows.

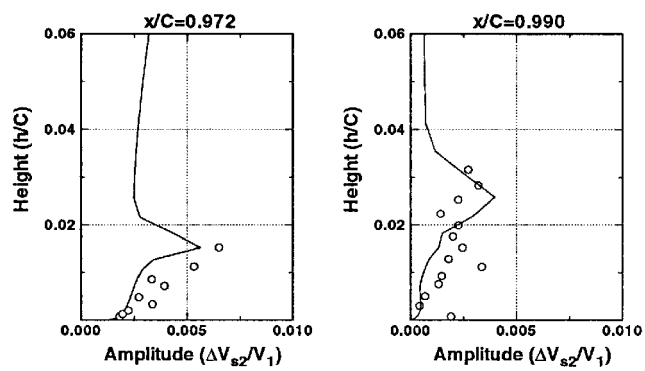

Pressure surface Suction surface

Fig. 15 Amplitude of the second harmonic of unsteady velocity on the hydrofoil (symbol, experimental data[7,20]).

The distribution of the time-mean turbulence kinetic energy on the blade suction surface is presented in Fig. 18. Equation (9) is used to calculate the time-mean values of the turbulence intensity T_u and the magnitude of the first harmonic. The turbulence intensity increases as the flow travels downstream. Near the trailing edge, the maximum turbulence intensity is as high as 9.5% of the inlet value, whereas in the freestream its value decreases to about 0.6–0.7% (compared to a 1% inlet turbulence intensity). Its range of influence also increases with the boundary-layer thickness. The influence of the boundary layer moves the peak of the time-mean turbulence intensity away from the surface. In Fig. 19, the peaks in the amplitude of ΔT_u occur exactly at the locations where the interaction between the boundary

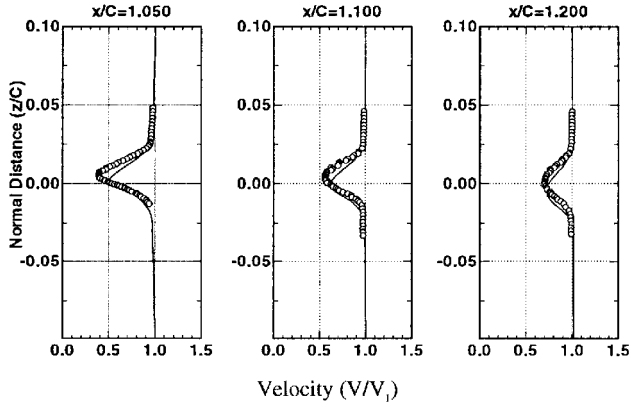

Fig. 16a Time-mean velocity downstream of the hydrofoil (symbol, steady-state measurement by Keenan et al.[7]).

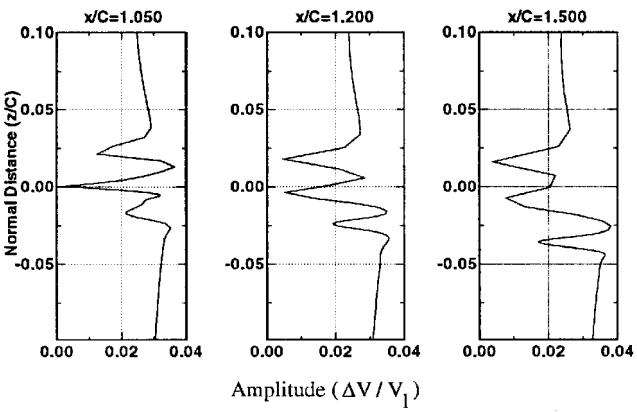

Fig. 16b Amplitude of the first harmonic of unsteady velocity downstream of the hydrofoil.

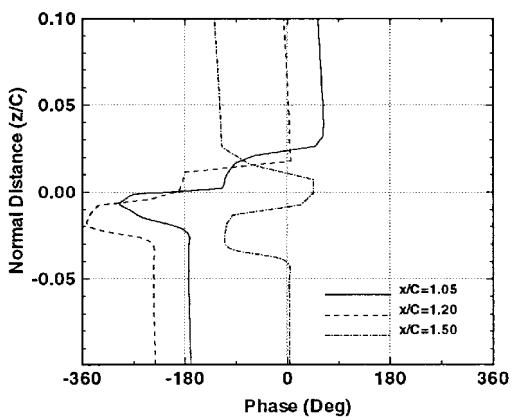

Fig. 16c Phase angle of the first harmonic of unsteady velocity downstream of the hydrofoil.

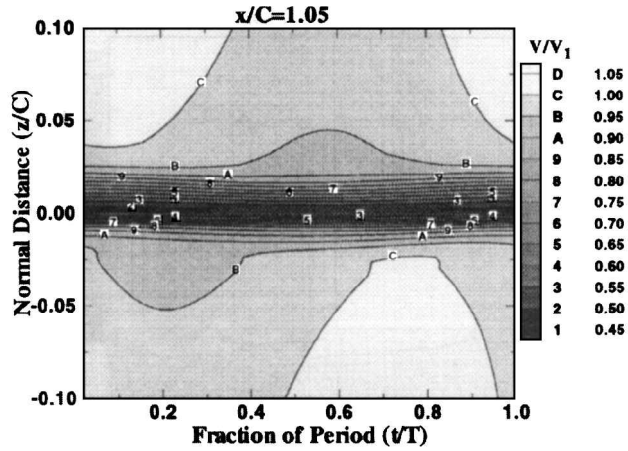

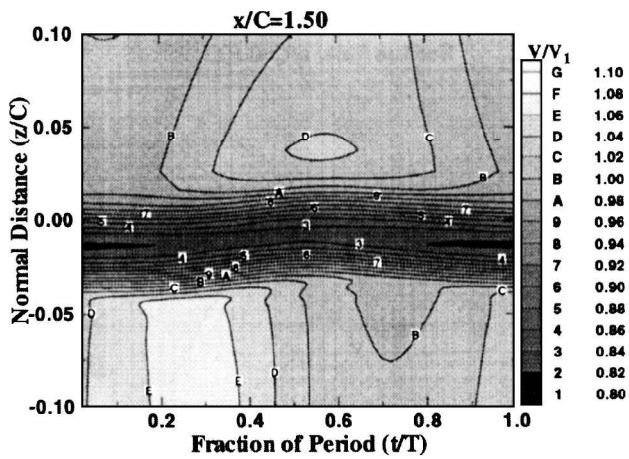

Fig. 17 Time history of the velocity downstream of the hydrofoil.

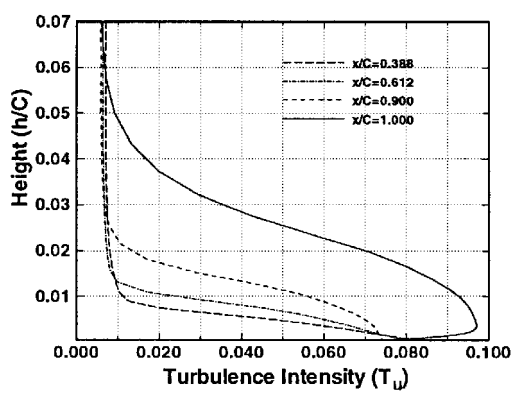

Fig. 18 Time-mean turbulence intensity T_u profiles on the suction surface of the hydrofoil.

layer and the freestream takes place (Figs. 9 and 10). A higher amplitude of ΔT_u corresponds to a lower amplitude of velocity fluctuation ΔV_s (see Fig. 9). Very close to the wall, because of the interaction between the turbulence and the wall, the amplitude of ΔT_u also increases. This phenomenon is particularly noticeable at the trailing edge; however, it does not show any visible effect on the magnitude of the velocity fluctuations. The phase-angle distributions of ΔT_u on the suction side, shown in Fig. 20, indicate a different behavior from that observed for the unsteady velocity. Instead of a phase lag (from the freestream values) inside the boundary layer due to a slower local velocity, the phase-angle distribution of turbulent intensity has a phase lead inside the boundary layer. This implies that the wall has a stronger influence on the turbulence. But, as the flow reaches the trailing edge, the influence of the boundary layer becomes evident. The phase-angle distribution inside the boundary layer lags behind that of the freestream. Nevertheless, the wall effect on the turbulence still can be seen from a small dip near the wall at the trailing edge region.

On the pressure surface, the distribution of the time-mean T_u is very similar to that of a flat plate. The amplitude and phase angle of the first harmonic for T_u shows behavior very similar to that on the suction side. These results can be found in Ho.[10] The time history of T_u on the suction side of the hydrofoil is shown at a location $x/C = 0.99$ in Fig. 21. The wall effect on the turbulence can be seen from $h/C = 0.05$ to 0.015. The magnitude of T_u is much higher in this region, and the phase angle is quite different from the freestream distribution.

The amplitude of the fluctuation in turbulence intensity, shown in Fig. 22, indicates two peaks on either side of the wake centerline. Note that the magnitude of the peak on the suction side decays as

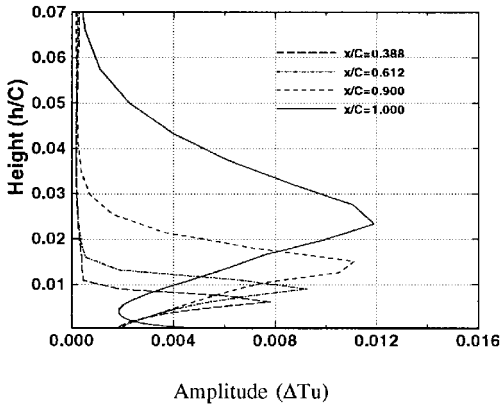

Fig. 19 Amplitude of the first harmonic of turbulence intensity ΔT_u on the suction surface of the hydrofoil.

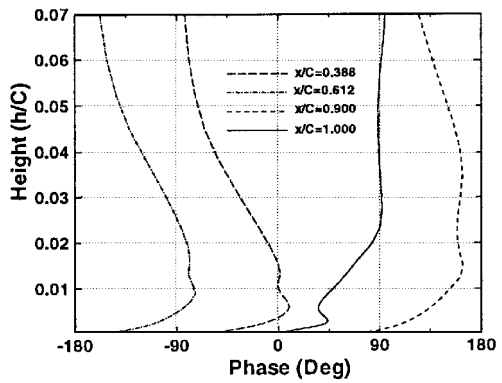

Fig. 20 Phase angle of the first harmonic of turbulence intensity ΔT_u on the suction surface of the hydrofoil.

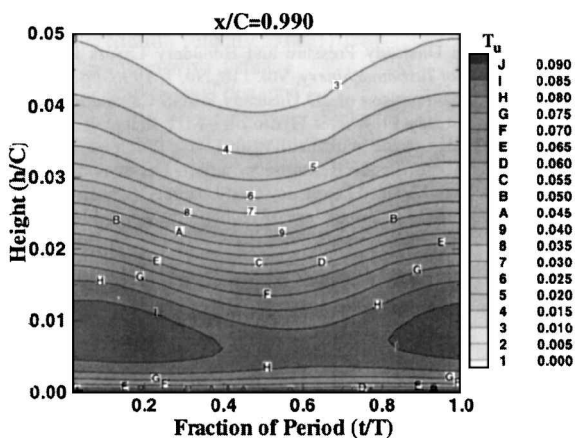

Fig. 21 Time history of turbulence intensity T_u distribution on the suction surface of the hydrofoil.

the wake travels downstream, whereas that of the pressure side increases its magnitude. An explanation for this curious behavior is that the interaction between the wake and the freestream vortex on the pressure (lower) side increases the turbulence (similar to the behavior that occurs at the edge of the boundary layers). On the suction (upper) side, the local velocity decreases as the flow pass the trailing edge, and this diffusion process dissipates the turbulence. The phase-angle distribution (Fig. 23) also indicates that a strong interaction occurs between the wake and the freestream. Figure 24 is the time history of the turbulence intensity downstream of the hydrofoil at $x/C = 1.50$. An interesting phenomenon can be observed in this plot. Comparing this figure with Fig. 17, it is clear that the freestream unsteadiness affects the high turbulence intensity patches and is almost in phase with the velocity fluctuations (compare Figs. 16c and 23). This occurs only in the far-wake and not in the near-wake region. This can be seen from a comparison

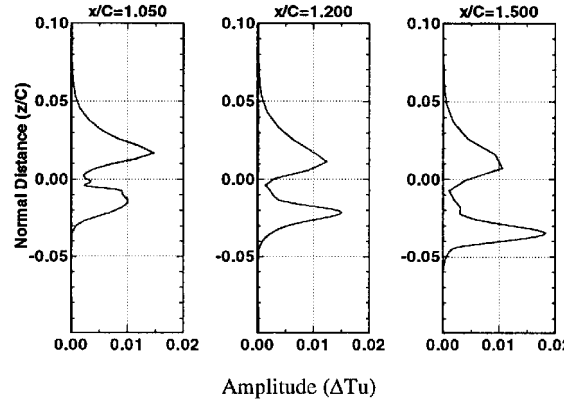

Fig. 22 Amplitude of the first harmonic of turbulence intensity T_u downstream of the hydrofoil.

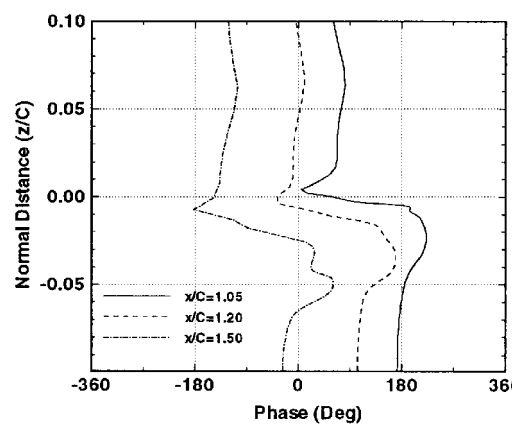

Fig. 23 Phase angle of the first harmonic of turbulence intensity T_u downstream of the hydrofoil.

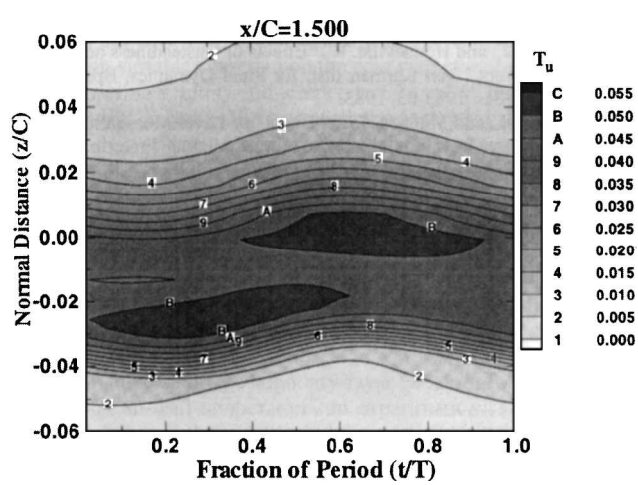

Fig. 24 Time history of turbulence intensity T_u distribution downstream of the hydrofoil.

of the phase angle of the velocity fluctuations at $x/C = 1.05$ and 1.50, shown in Fig. 16c, with the turbulence intensity fluctuations at these locations, shown in Fig. 23. This seems to indicate that the unsteady wake far downstream (after $x/C = 1.50$ in this case) has achieved an equilibrium condition.

Concluding Remarks

A two-dimensional, unsteady, Navier–Stokes code has been used to compute the unsteady flow over a hydrofoil stimulated by two upstream flapping foils. The agreement between the computation and the experimental data is very good, including the amplitude and phase angle of the unsteady velocity. It is found that the unsteady

flow outside the boundary layer is dominated by the vortices shed from the upstream flapping foils. The flow inside the boundary layer is controlled by the vortices due to the unsteady flow traveling inside the boundary layer and the fluctuating pressure gradient on the foil surface. These vortices travel along the hydrofoil surfaces with the local velocity. Therefore, there are distinct phase changes across the edge of the boundary layer. The interaction between these two flow patterns reduces the unsteadiness at the edge of the boundary layer. This interaction also increases the amplitude of the turbulence kinetic energy at the edge of the boundary layer.

The first harmonic of the unsteady velocity inside the boundary layer is found to have dominant effect on the flowfield. At the edge of the boundary layer, a small portion of the energy is being transferred to the higher harmonics, which causes the reduction in unsteadiness.

The unsteadiness inside the boundary layer is carried farther downstream into the wake region. The velocity fluctuations in the freestream interact strongly with the wake. The interaction between these vortices and the wake increases the unsteadiness on both sides of the wake. The flow pattern inside the wake, however, still is dominated by viscous effects. The phase-angle differences between the velocity fluctuations and the turbulence kinetic energy become smaller as the flow travels downstream. It is found that the unsteady wake achieves an equilibrium condition at about 50% downstream of the hydrofoil.

Acknowledgment

This work is supported by the Office of Naval Research through Contract N00014-90-J1182 with J. Fein as the Contract Monitor. The authors would like to thank P. J. Morris and D. E. Thompson for their helpful suggestions and D. Keenan for providing the experimental data. The authors also wish to acknowledge NASA for providing the supercomputing resources at the National Aerodynamic Simulation Facility at NASA Ames Research Center and at NASA Lewis Research Center.

References

[1]Patel, M. H., "On Turbulent Boundary Layers in Oscillatory Flow," *Proceedings of the Royal Society of London, Series A: Mathematical and Physical Sciences*, Vol. 353, 1977, pp. 121–144.

[2]Cousteix, J., and Houdeville, R., "Effects of Unsteadiness on Turbulent Boundary Layers," Von Kármán Inst. for Fluid Dynamics, Brussels, Belgium, Lecture Ser. 1983-03, 1983.

[3]Brendel, M., and Mueller, T. J., "Boundary-Layer Measurements on an Airfoil at a Low Reynolds Number in an Oscillating Freestream," *AIAA Journal*, Vol. 26, No. 3, 1988, pp. 257–263.

[4]Huff, D. L., "Numerical Simulation of Unsteady, Viscous, Transonic Flow over Isolated and Cascaded Airfoils Using a Deforming Grid," AIAA Paper 87-1316, 1987.

[5]Scott, J. R., and Atassi, H. M., "Numerical Solution of Periodic Vortical Flows About a Thin Airfoil," NASA TM-101998, 1989.

[6]Ghia, K. N., Yang, J., Osswald, G. A., and Ghia, U., "Study of the Dynamic Stall Mechanism Using Simulation of Two-Dimensional Navier–Stokes Equations," AIAA Paper 91-0546, 1991.

[7]Keenan, D. P., Lurie, E. H., Mazel, C. A., and Kerwin, J. E., "Experimental Study of the Boundary Layer on a Hydrofoil Subject to Periodic Gusts," Ocean Engineering Dept., Massachusetts Inst. of Technology, Cambridge, MA, 1993.

[8]Chien, K.-Y., "Prediction of Channel and Boundary-Layer Flows with a Low-Reynolds-Number Turbulence Model," *AIAA Journal*, Vol. 20, No. 1, 1982, pp. 33–38.

[9]Patel, V. C., Rodi, W., and Scheuerer, G., "Turbulence Models for Near-Wall and Low Reynolds Number Flows: A Review," *AIAA Journal*, Vol. 23, No. 9, 1985, pp. 1308–1319.

[10]Ho, Y.-H., "Numerical Simulation of Steady and Unsteady Viscous Flows in Turbomachinery Blade Rows," Ph.D. Thesis, Dept. of Aerospace Engineering, Pennsylvania State Univ., University Park, PA, 1995.

[11]Basson, A. H., and Lakshminarayana, B., "An Artificial Dissipation Formulation for Semi-Implicit Pressure Based Solution Scheme for Viscous and Inviscid Flows," *International Journal of Computational Fluid Dynamics*, Vol. 2, 1994, pp. 253–282.

[12]Issa, R. I., "Solution of the Implicitly Discretized Fluid Flow Equations by Operator-Splitting," *Journal of Computational Physics*, Vol. 62, 1985, pp. 40–65.

[13]Van Doormaal, J. P., and Raithby, G. D., "Enhancements of the SIMPLE Method for Predicting Incompressible Fluid Flows," *Numerical Heat Transfer*, Vol. 7, 1984, pp. 147–163.

[14]Justesen, P., and Spalart, P. R., "Two-Equation Turbulence Modeling of Oscillatory Boundary Layer," AIAA Paper 90-0496, 1990.

[15]Fan, S., Lakshminarayana, B., and Barnett, M., "A Low-Reynolds-Number k-ε Model for Unsteady Turbulent Boundary-Layer Flows," *AIAA Journal*, Vol. 31, No. 10, 1993, pp. 1777–1784.

[16]Mankbadi, R. R., and Mobark, A., "Quasi-Steady Turbulence Modeling of Unsteady Flows," *International Journal of Heat Transfer and Fluid Flow*, Vol. 12, 1991, pp. 122–129.

[17]Jones, W. P., and Launder, B. E., "The Prediction of Laminarization with a Two Equation Model of Turbulence," *International Journal of Heat and Mass Transfer*, Vol. 15, 1972, pp. 301–314.

[18]Fan, S., and Lakshminarayana, B., "Computation and Simulation of Wake Generated Unsteady Pressure and Boundary Layers in Cascades, Part 1," *Journal of Turbomachinery*, Vol. 118, No. 1, 1996, pp. 96–108.

[19]Fuhs, D., "Comparison of 2D Unsteady RANS Calculation and Measurement of Unsteady Flow over Hydrofoil—MIT Flapping Foil Experiment," NSWC Rept. (to be published).

[20]Lurie, E. H., "Unsteady Response of a Two Dimensional Hydrofoil Subjected to a High Reduced Frequency Gust Loading," Ocean Engineering Dept., Rept. 93-5, Massachusetts Inst. of Technology, Cambridge, MA, June 1993 (also see Rept. 96-4, Sept. 1996).